Available online at www.sciencedirect.com
ScienceDirect
Trans. Nonferrous Met. Soc. China 35(2025) 3043−3056
Transactions of Nonferrous Metals Society of China
www.tnmsc.cn

AIMD study on correlation between chemical effects and segregation behavior in liquid Sb-based alloy

Zong-bo LI[1,2], Yan FENG[1,2], Ze-hang ZHUANG[1,2], Xiang PENG[1,2], Ri-chu WANG[1,2]

1. School of Materials Science and Engineering, Central South University, Changsha 410083, China;
2. National Key Laboratory of Science and Technology on High-strength Structural Materials, Central South University, Changsha 410083, China

Received 14 March 2025; accepted 16 September 2025

Abstract: Elements (As, Bi) and (Cu, Fe) exhibiting two typical segregation behavior in liquid Sb alloys were selected as solute atoms for analysis. Ab initio molecular dynamics (AIMD) simulations were employed to study the molten Sb alloy at different temperatures. By analyzing its pair correlation function (PCF), bond pairs, bond angle distribution function (BADF), and Voronoi polyhedron (VP), the short-range order (SRO) of the alloy was investigated. In the Sb melt, the solute atoms Cu and Fe, which have smaller distribution coefficients, exhibit a stronger affinity for Sb than the solute atoms As and Bi, which have larger distribution coefficients. The BADF of As and Bi with larger distribution coefficients shows a lower probability of small-angle peaks compared to large-angle peaks, whereas the BADF of Cu and Fe with smaller distribution coefficients exhibits the opposite trend. The BADF reveals that Sb−As and Sb−Bi approach pure Sb melt, while Sb−Cu and Sb−Fe deviate significantly. Compared to Sb−Cu and Sb−Fe, the Sb−As and Sb−Bi systems exhibit more low-index bonds, suggesting weaker interactions and more disorder. The VP fractions around As and Bi atoms are lower than those around Cu and Fe, and the VP face distributions around As and Bi are more complex. There are differences in the VP around different solute atoms, primarily due to the varying bond pair fractions associated with each solute atom. Fe has the smallest diffusion coefficient, primarily due to its compact local structure.

Key words: AIMD; segregation; liquid Sb-based alloys; short-range order; As; Bi; Cu; Fe

1 Introduction

Antimony, as a critical material in the fields of semiconductor and thermoelectrics, has attracted significant research attention due to its unique physical and chemical properties [1,2]. High-purity Sb is especially important for these applications, as impurity elements can significantly influence its performance [3]. The preparation of high-purity metallic antimony typically requires a combination of chemical and physical methods [4]. Ultimately, zone refining is often employed as the final step to achieve high-purity antimony. However, achieving high-purity Sb faces a fundamental challenge: conventional segregation methods are ineffective at removing impurity elements such as As, which exhibits a partition coefficient near 1 in liquid Sb [5]. These impurities tend to remain uniformly distributed in the melt, thereby limiting the efficiency of purification techniques [6].

Currently, numerous studies have been reported on the removal of impurities from high-purity antimony [7−9]. ZHENG et al [10] investigated a predictive model for impurity concentration in high-purity Sb during the vacuum

Corresponding author: Yan FENG, Tel +86-13755199741, E-mail: fengyanmse@csu.edu.cn;
Xiang PENG, Tel +86-18975157936, E-mail: pengxiang@csu.edu.cn
https://doi.org/10.1016/S1003-6326(25)66865-8

distillation, based on solute mass conservation, accurately describing the exponential decrease of As and increase of Bi in the residue, as well as their distinct concentration gradients in the distillate. MENG et al [3] introduced two vacuum distillation processes (LHVD and HLVD) for removing trace impurities from crude antimony. LHVD outperforms HLVD in impurity removal, yielding antimony with 99.9961 wt.% in purity and impurity content of 3.9×10^{-5}, compared to 99.9947 wt.% and 5.294×10^{-5} for HLVD. ZHANG et al [11] studied zone refining of Sb for As removal and process optimization using numerical simulations. Limited As evaporation under inert gas flux highlighted the need for pre-treatment. Zone refining experiments and Spim/BPS models determined effective distribution coefficients and diffusion ratios, enabling precise predictions of purification efficiency and refining parameters. Experimental studies and numerical simulations have been focused on optimizing purification methods, such as improving the efficiency of zone refining or developing alternative techniques to remove impurities like As. These studies have also shed light on the thermodynamic and kinetic properties of Sb melts, providing valuable insights into the behavior of impurities during purification processes. However, while experimental approaches offer macroscopic observations, they lack the ability to reveal the atomic-scale structural and chemical mechanisms governing impurity behavior in liquid Sb. Ab initio molecular dynamics (AIMD) simulations have become a powerful tool for exploring the structural and dynamical properties of liquid metals and alloys at the atomic level [12,13]. For Sb, AIMD studies have provided preliminary insights into its liquid structure and bonding characteristics. HAO et al [14] used AIMD of liquid pure Sb (913−1193 K) to reveal the residual crystalline structures and an anomalous structural change around 1023 K, marked by variations in $S(q)$, cluster properties, and bond order parameters.

Despite these efforts, the correlation between the chemical effects of solute atoms and their segregation behavior in liquid Sb remains poorly understood. Particularly, the atomic-scale structural characteristics of solute-centered environments in the melt, which play a crucial role in determining impurity behavior, have yet not to be thoroughly investigated. Specifically, structural configurations around solute atoms, such as As, Bi, Fe, and Cu, and their impact on impurity distribution have yet not to be thoroughly investigated. To address this gap, the present study conducts an AIMD investigation into the relationship between chemical effects and segregation behavior in Sb-based liquid alloys. By focusing on high-purity Sb, this research aims to unravel the solute-centered local structural features in the melt and their implications for impurity behavior. Specifically, the bond angle distribution function, Voronoi polyhedron (VP) configurations surrounding solute atoms, and dynamical properties are analyzed, to gain insights into their atomic-scale distribution and interactions within the Sb melt. This work explores the link between local chemical environments and impurity segregation in liquid Sb, offering insights to improve purification strategies and guide the design of high-purity Sb materials and Sb-based alloys.

2 Computational details

In this study, AIMD [15] simulations were performed using the Vienna ab initio simulation package (VASP) [16], based on the density functional theory (DFT) [17]. The interactions between electrons and ions were treated using the projector augmented wave (PAW) [18] method, while electronic exchange and correlation effects were described using the Perdew-Burke-Ernzerhof (PBE) [19] functional within the generalized gradient approximation (GGA) [20]. All the simulations were conducted in the NVT ensemble [21], with temperature controlled by the Nosé-Hoover [22] thermostat to maintain the desired conditions. The plane-wave energy cutoff was set to be 270 eV [23], and k-point sampling was restricted to the Γ-point of Brillouin zone, with a time step of 3 fs [24,25]. To ensure stable pressure conditions, the “zero external pressure” [26] method was employed, keeping the absolute value of the total pressure below 0.2 GPa [27]. Table 1 presents the supercell dimensions and the corresponding densities of the system obtained at different temperatures. The electronic structure calculations were performed using a 3×3×3 k-point grid to ensure adequate k-point convergence.

In all simulations, the initial configuration consisted of a cubic supercell containing 108 atoms, including 88 Sb atoms and 20 solute atoms randomly

Table 1 Supercell dimensions and corresponding densities of systems obtained at different temperatures

Temperature/K	$Sb_{88}As_{20}$		$Sb_{88}Bi_{20}$		$Sb_{88}Cu_{20}$		$Sb_{88}Fe_{20}$	
	Length/Å	Density/(g·cm^{-3})	Length/Å	Density/(g·cm^{-3})	Length/Å	Density/(g·cm^{-3})	Length/Å	Density/(g·cm^{-3})
1600	15.13	5.858	15.89	6.167	15.20	5.681	15.24	5.552
1500	15.06	5.939	15.81	6.261	15.15	5.725	15.14	5.663
1400	14.96	6.059	15.74	6.345	15.08	5.806	15.08	5.731
1300	14.87	6.170	15.67	6.430	15.00	5.899	15.01	5.812

distributed within the cell. The periodic boundary conditions were applied. Configuration of the liquid $Sb_{88}X_{20}$ (X=Fe, Cu, As, Bi) alloy supercells is illustrated in Fig. 1. To minimize the influence of the initial structure on the results, each system was first relaxed for 2000 steps at 2000 K. The system was then gradually cooled down to 1600, 1500, 1400, and 1300 K, with a cooling rate of 4.44×10^{13} K/s. Subsequently, molecular dynamics (MD) simulations were performed for 10000 steps at each target temperature. The data from the last 5000 steps were analyzed to determine the local structure and dynamic properties of the melt.

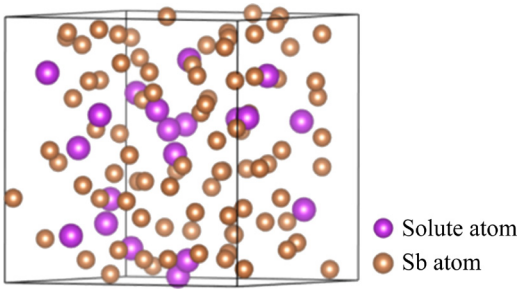

Fig. 1 Supercell structure of $Sb_{88}X_{20}$ (X = Fe, Cu, As, Bi) consisting of Sb atoms, represented by yellow spheres, and solute atoms, depicted in violet

3 Results and discussion

3.1 Static structure factors

The static partial structure factors and the total structure factor of a binary liquid metal system are calculated based on Eqs. (1) and (2), respectively [24,28]:

$$S_{\text{partial}}(q)=\frac{1}{\sqrt{N_\alpha N_\beta}}\sum_{i=1}^{N_\alpha}\sum_{j=1}^{N_\beta}\exp[-\mathrm{i}q(\boldsymbol{r}_{i,\alpha}-\boldsymbol{r}_{j,\beta})] \quad (1)$$

$$S_{\text{total}}(q)=\frac{c_\alpha b_\alpha^2 S_{\alpha\alpha}(q)+2\sqrt{c_\alpha c_\beta}b_\alpha b_\beta S_{\alpha\beta}(q)+c_\beta b_\beta^2 S_{\beta\beta}(q)}{c_\alpha b_\alpha^2+c_\beta b_\beta^2} \quad (2)$$

where N_α and N_β represent the number of atoms of different types in the binary system, while $\boldsymbol{r}_{i,\alpha}$ and $\boldsymbol{r}_{i,\beta}$ denote the position vectors. The wave vector in reciprocal space is given by $q=(2\pi/L)(n_x, n_y, n_z)$, here L is the length of the supercell, and n_x, n_y, n_z are integers. c_α and c_β represent the atomic densities, and b_α and b_β are the neutron scattering lengths corresponding to each atomic species. Angular brackets denote the time-averaged values.

Figure 2 shows the static structure factors of $Sb_{88}X_{20}$ measured at 1600 K. Figure 2 reveals that the first peak intensity of total structure factors for $Sb_{88}X_{20}$ (X=As, Bi, Cu, Fe) exhibits a significant reduction. This indicates that the incorporation of Cu and Fe induces stronger chemical and structural perturbations than As and Bi, resulting in reduced structural ordering and a more pronounced decrease in the first peak intensity. A characteristic pre-peak is observed in the range of 1−2 Å^{-1} for the $Sb_{88}As_{20}$ melt, indicating the presence of chemical ordering in the liquid state. This phenomenon is analogous to the pre-peaks previously documented in Zr−Ni [29] and Al−Fe [30] liquid systems. The appearance of the pre-peak reflects chemical ordering in the structure, which leads to local inhomogeneity in

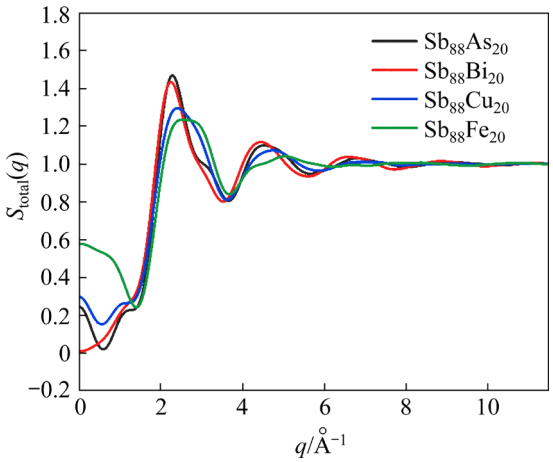

Fig. 2 Total structure factors of $Sb_{88}As_{20}$, $Sb_{88}Bi_{20}$, $Sb_{88}Cu_{20}$ and $Sb_{88}Fe_{20}$ at 1600 K

charge distribution, thus stabilizing or promoting the uniqueness of local structures.

Consequently, the first peak positions shift gradually to the right. In other words, when Sb atoms coordinate with Cu or Fe atoms, Cu and Fe atoms tend to approach Sb atoms more closely, leading to shorter average distances for Sb−Cu and Sb−Fe pairs.

3.2 Pair-correlation function (PCF)

The PCF is a function that describes the relative position distribution of particles in a material. It is commonly used to study the microstructure of liquids, gases, and amorphous materials. The common expression is as follows [26,31]:

$$g(r)=\frac{l^3}{N_A N_B}\left\langle\sum_{i=1}^{N_A}\frac{n_{iB}(r,\Delta r)}{4\pi r^2\Delta r}\right\rangle \tag{3}$$

where the length of the supercell is denoted as l, the total number of A atoms is represented by N_A, and the total number of B atoms is represented by N_B. As for $n_{iB}(r,\Delta r)$, it specifically describes the situation where the number of B atoms is counted within a spherical shell region centered on any A atom (denoted as the i-th atom) with a radius extending from r to $r+\Delta r$.

Figure 3 shows the partial PCFs of Sb−X (X=As, Bi, Cu, Fe) melts at 1600K. From Fig. 3(a), a clear difference can be seen in the height of the first peak in Sb−X melt. The first peak intensities of Sb−As and Sb−Bi are relatively similar, while the first peak intensities of Sb−Cu and Sb−Fe are significantly enhanced. Among them, the interaction between Sb and Fe is particularly strong. This suggests that around Sb−Fe, the local atomic arrangement is more compact, and the chemical bonds are stronger, which enhances the short-range order. Therefore, the strong interaction between Sb and Fe, along with the resulting local structural changes, is the primary reason for the maximum intensity of the first peak in $g_{Sb-Fe}(r)$. The position of the first peak is related to the equilibrium bond length between atoms. As shown in Fig. 3(b), the bond lengths increase in the order of Sb—Fe, Sb—Cu, Sb—As, and Sb—Bi. In Sb−X binary melts with a high solute content, there are three types of interactions: Sb−Sb, Sb−X, and X−X interactions. These interactions collectively influence the local structures around both the solvent and solute atoms in the melt. The formation of local structures and other melt properties are caused by the competition among these three interactions.

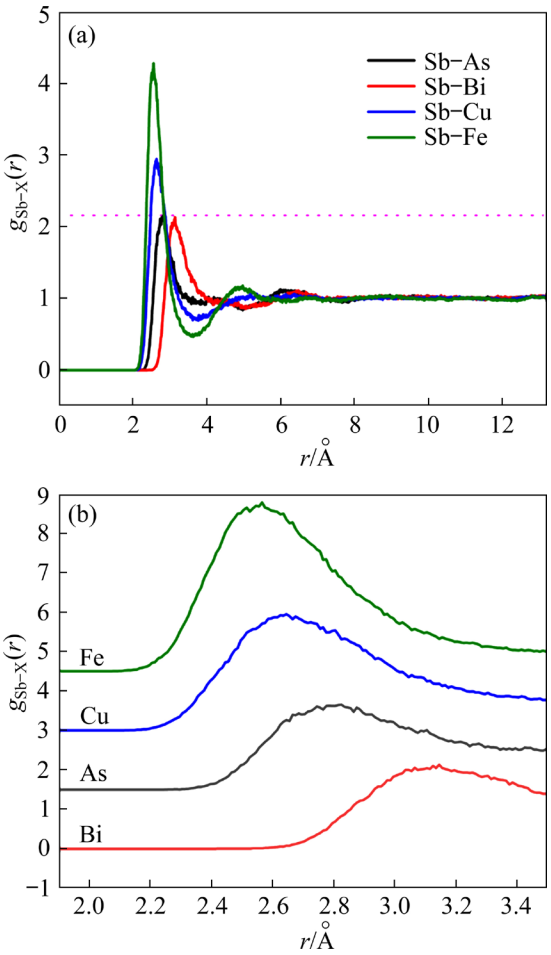

Fig. 3 (a) Partial PCF of Sb−X (X=As, Bi, Cu, Fe) melt at 1600 K; (b) Values of different systems on same number line exhibiting difference of one unit along y-axis

From Fig. 4(a), in Sb−As system, the intensity of the first peak of $g_{As-As}(r)$ is significantly higher than that of $g_{Sb-Sb}(r)$ and $g_{Sb-As}(r)$, indicating that the As−As interaction is the strongest in the Sb−As system. This suggests that As atoms tend to bond with each other and form clusters. In Fig. 4(b), for the Sb−Bi system, the first peak intensities of $g_{Sb-Sb}(r)$ and $g_{Sb-Bi}(r)$ are almost the same, but both are higher than that of $g_{Bi-Bi}(r)$. This suggests that the Bi−Bi interaction is the weakest in the Sb−Bi system, and Bi atoms preferentially bond with Sb atoms. In Fig. 4(c), for the Sb−Cu system, the first peak intensity follows the order $g_{Sb-Cu}(r) > g_{Cu-Cu}(r) > g_{Sb-Sb}(r)$, indicating that in the Sb−Cu

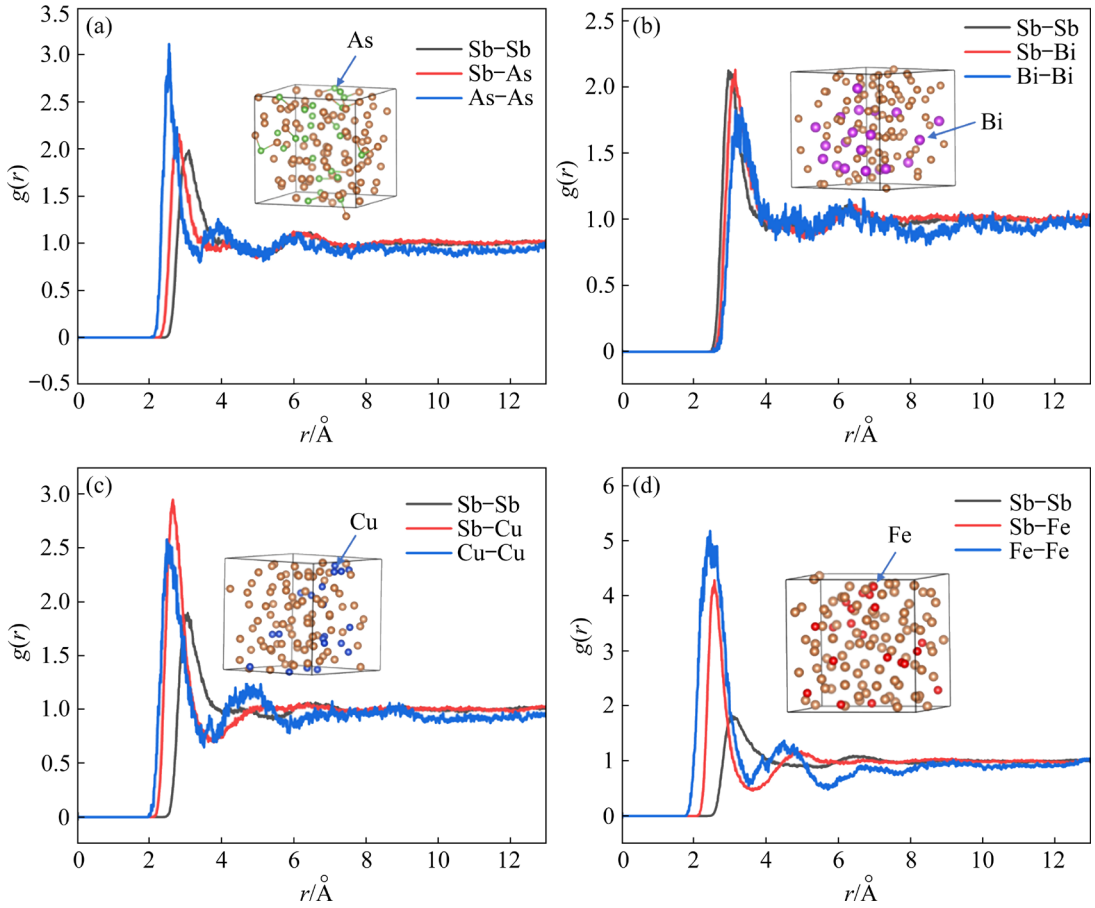

Fig. 4 Partial PCF of $Sb_{88}X_{20}$ (X=As, Bi, Cu, Fe) melt at 1600 K

system, Cu atoms preferentially bond with Sb atoms, followed by self-bonding among Cu atoms. In Fig. 4(d), the Sb−Fe system, the first peak intensity of $g_{Sb-Sb}(r)$ is much lower than that of $g_{Sb-Fe}(r)$ and $g_{Fe-Fe}(r)$, with the first peak of $g_{Sb-Fe}(r)$ being slightly smaller than that of $g_{Fe-Fe}(r)$. This suggests that Fe atoms preferentially bond with themselves, but they also show a strong bonding tendency when interacting with Sb atoms. The different bonding characteristics in different system lead to distinct microscopic structural properties. It is noteworthy that in all the systems, the peak of $g_{Sb-Sb}(r)$ is almost identical, with no significant difference in either the peak position or intensity. This indicates that adding different types of solute elements to the Sb alloy melt does not significantly affect the Sb−Sb interaction.

3.3 Coordination number and chemical ordering parameter

The coordination number (CN) of a melt refers to the number of directly neighboring atoms surrounding a single atom in a liquid metal or alloy. As a key parameter for describing the local atomic structure, the coordination number helps to understand the arrangement and interactions of atoms in the melt. By utilizing the PCF, the partial CN [27] for different systems can be calculated. In this work, a statistical analysis of the partial CN around the central Sb atoms and solute atoms in four systems at different temperatures is shown in Fig. 5.

Studies on different alloy systems have shown that temperature significantly affects the CN and atomic distribution [32]. As shown in Fig. 5(a) for the Sb−As alloy solution, the CN of Sb atoms decreases with increasing temperature, and the number of Sb atoms around As atoms also decreases as the temperature rises. However, the number of As atoms around As atoms increases with increasing temperature. This indicates that, as the temperature increases, the total CN of the alloy decreases, the chemical short-range order weakens, and As atoms tend to cluster with the same type atoms. Next, for the Sb−Bi alloy solution, as shown in Fig. 5(b), the CN decreases with increasing

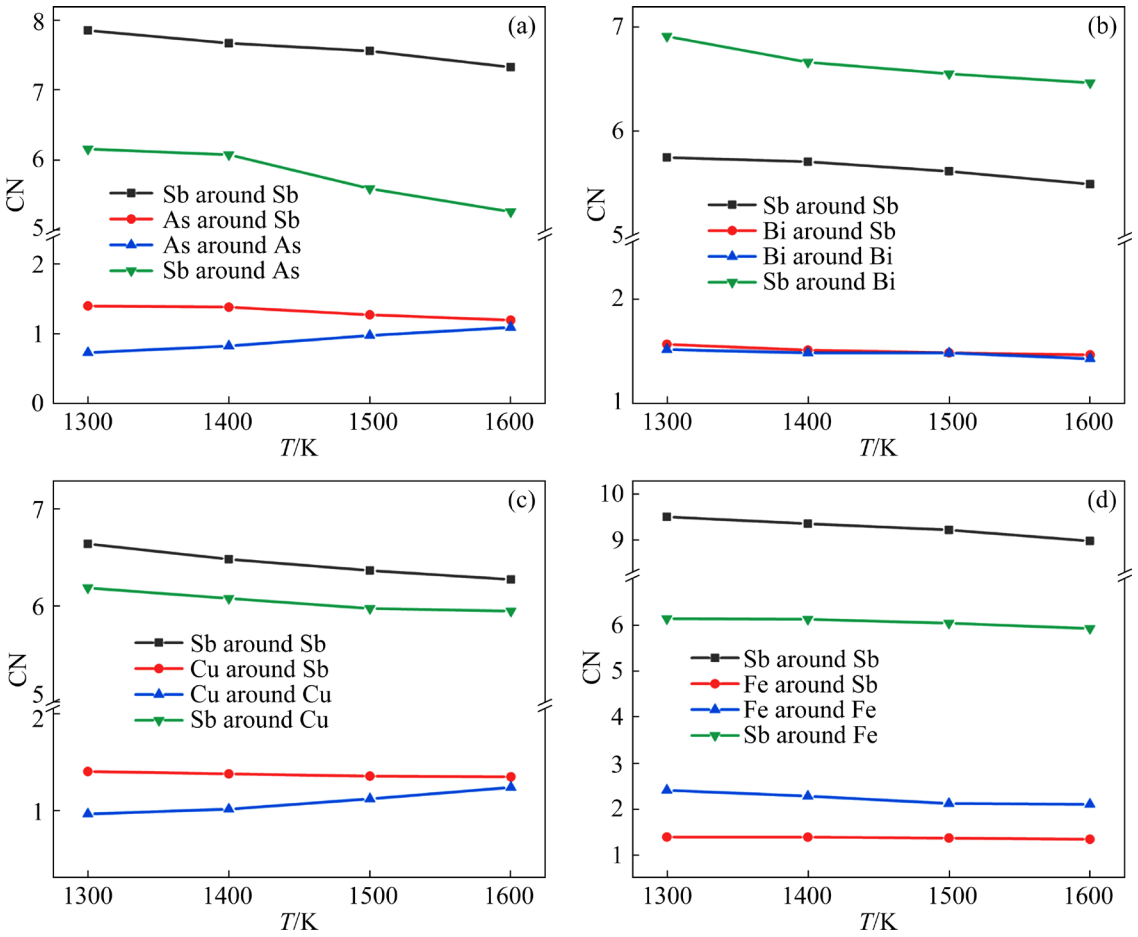

Fig. 5 Partial CN of liquid Sb−As (a), Sb−Bi (b), Sb−Cu (c), and Sb−Fe (d) alloys at different temperatures

temperature. The number of Bi atoms around Sb atoms is nearly the same as the number of Bi atoms around other Bi atoms, indicating that as the temperature rises, the CN decreases and there is no clear bonding preference for Bi atoms. This suggests a decrease in chemical short-range order with increasing temperature.

For the Sb−Cu alloy solution, as shown in Fig. 5(c), the CN of Sb atoms increases as the temperature decreases. The number of Sb atoms around Cu atoms increases, while the number of Cu atoms around Cu atoms decreases. This indicates that as the temperature decreases, the CN increases, the chemical short-range order improves, and Cu atoms tend to bond with Sb atoms. Finally, for the Sb−Fe alloy solution shown in Fig. 5(d), the CN also gradually decreases with increasing temperature. In the Sb−Fe melt, the number of Fe atoms around Fe atoms is higher than the number of Fe atoms around Sb atoms. This suggests that Fe atoms tend to cluster around themselves, and the number of atoms surrounding Fe is greater than that around other solute species. This implies that the "cage" structure formed around Fe atoms is relatively dense, with distinct characteristics of chemical short-range order.

The Warren−Cowley (W−C) model defines a short-range order parameter α_{ij} to quantify the interaction between different types of atoms in the lattice. The definition is as follows [33,34]:

$$\alpha_{ij}=1-\frac{\mathrm{CN}_{ij}}{x_j\left(x_i\mathrm{CN}_j+x_j\mathrm{CN}_i\right)} \tag{4}$$

where CN_i is the sum of CN_{ii} and CN_{ij}, while x_i and x_j represent the concentrations of elements i and j, respectively. When the W−C parameter is negative, it indicates a bonding tendency between atoms i and j. When the W−C parameter is positive, it suggests that atoms i and j tend to be non-bonding. Figure 6 illustrates the variation of W−C chemical order parameters with temperature. As demonstrated in Fig. 6, the α_{ij} values progressively decrease with decreasing temperature. This suggests that the chemical short-range order in the liquid Sb−X

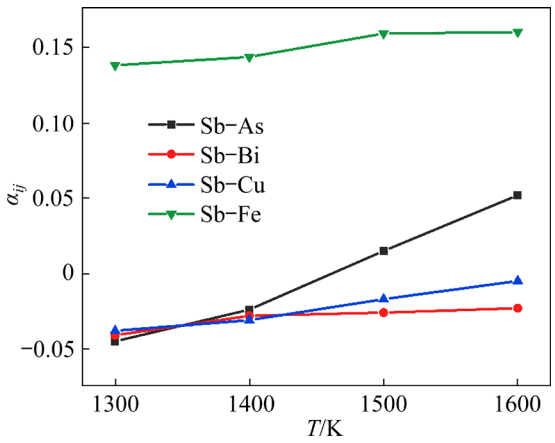

Fig. 6 Variation of W−C parameters with temperature for liquid Sb−As, Sb−Bi, Sb−Cu, and Sb−Fe alloys

(X=As, Bi, Cu, Fe) alloy intensifies as the temperature decreases, accompanied by an increasingly pronounced tendency for atomic bonding.

3.4 Honeycutt–Andersen index analysis

Honeycutt and Andersen introduced the bond pair analysis methodology. This approach enables the identification of various types of chemical bonds and interactions present in a solution, thereby providing a deeper understanding of microscopic structure. The bond pairs are characterized using four indices, denoted as "*ijkl*," with the definitions of these indices aligning with those established in the literature [35,36].

In the Sb−X binary systems, two approaches are used for analyzing the nearest-neighbor bonds: one is based on the Sb−X root pair, and the other on the X−X root pair. In this system, the fraction of a particular bond type is defined as the ratio of the number of that bond type to the total number of bonds in the melt. This fraction reflects the probability of the existence of that bond type. Figure 7 shows the temperature dependence of the fractions of various bond types based on different root pairs in the Sb−As, Sb−Bi, Sb−Cu, and Sb−Fe systems (only bond types with a fraction greater than 0.05 are shown). It is found that, regardless of whether Sb−X (X=As, Bi, Cu) or X−X (X=As, Bi, Cu) is chosen as the root pair, the bond types 1311, 1211, 1311, and 1201 appear in all the systems. In the Sb−As and Sb−Bi systems, many low-index bond types, such as 1101 and 1001, are observed. Typically, low-index bond types tend to appear in systems with lower symmetry and weaker interactions. This phenomenon indicates that in the Sb−As and Sb−Bi alloy melts, the interactions between Sb−As and As−As, as well as Sb−Bi and Bi−Bi, are relatively weak. Moreover, these bond types may exhibit more disordered arrangements or form structures with lower degrees of short-range order.

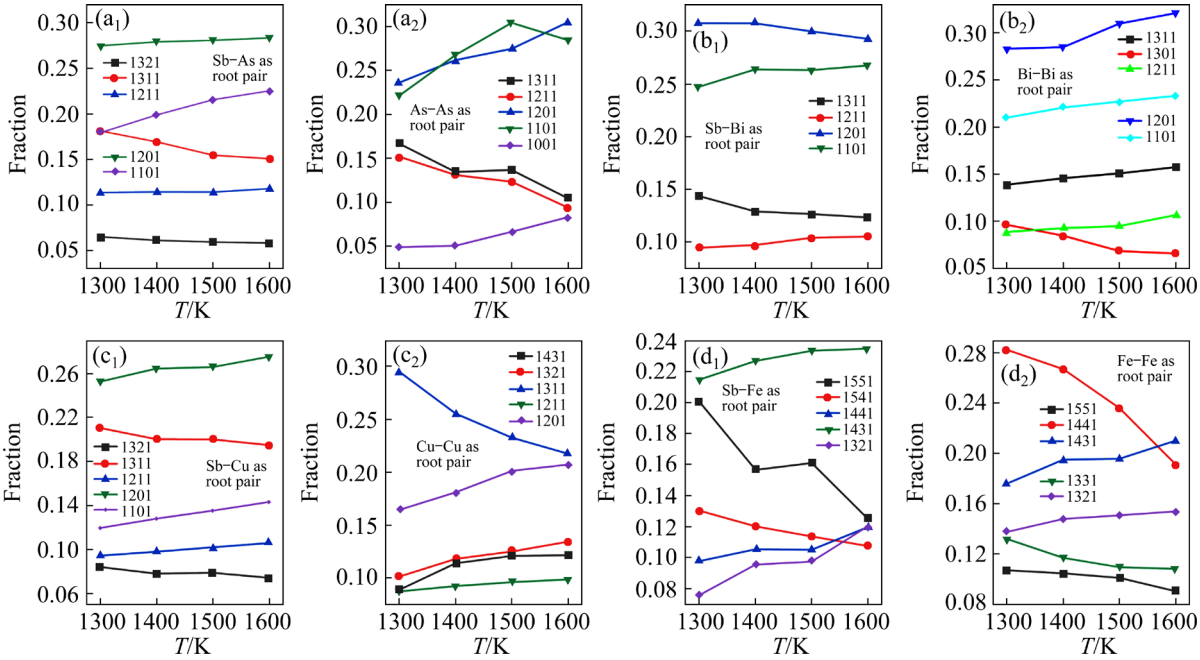

Fig. 7 Temperature-dependent fractions of different bonded pair types in molten Sb−As (a_1, a_2), Sb−Bi (b_1, b_2), Sb−Cu (c_1, c_2), and Sb−Fe (d_1, d_2) alloy

In the Sb−X binary systems, the 1551 bond pair with Sb−X as the root pair exhibits a unique distribution feature, which is only commonly observed in the Sb−Fe system. This 1551 bond pair can be regarded as a local five-fold symmetry (L-FFS) structure. According to the analysis in Section 3.2, there is a strong attraction between Sb and Fe, and the presence of the L-FFS structure in the Sb−Fe system. These two factors work together to promote the formation of a locally ordered structure around the Fe base. This local ordering around the Fe base slows down the motion of Fe atoms. Moreover, studies by CHENG et al [37] and FENG et al [38] have shown that a high proportion of F-FFS and L-FFS structures promotes the formation of compact clusters, which act as powerful “cages” that can hinder the diffusion of solute atoms. It can be inferred that in the Sb−Fe alloy melt, the L-FFS structure will inevitably impede the diffusion of Fe atoms. From the distribution of various bond types based on X−X as the root pair, no high-index bond pairs such as 1551 are detected in the Sb−As, Sb−Bi, and Sb−Cu systems. However, such bond pairs are detectable in the Sb−Fe system. This series of phenomena clearly reflect the significant impact that the differences in chemical bonding between different elements have on the local structure of the melt.

3.5 Bond-angle distribution function (BADF)

The BADF [39] describes the distribution of bond angles between a central atom and its neighboring bonded atoms. The triples aid in the analysis of specific topological order in solute atomic structures in the liquid. The triplets formed in this process are defined in the same way as mentioned in Ref. [21]. The positions of the first and second peaks correspond to the small bond angle (acute angle AA) and large bond angle (obtuse angle OA) formed between the central atom and its nearest neighbors, respectively, while the peak intensities reflect the probability of occurrence of the respective bond angles. To more clearly represent the orientational information of geometric configuration in the melt structure, this study performs statistical analysis on three types of bond angles in the melt: Sb—X—Sb, X—Sb—X, and X—X—X. Here, the Sb—X—Sb bond angle is defined as the angle formed by the solute atom as the vertex and the adjacent nearest Sb atoms. The definitions of the X—Sb—X and X—X—X bond angles are analogous to that of the Sb—X—Sb bond angle. The corresponding bond angle distribution functions are shown in Fig. 8.

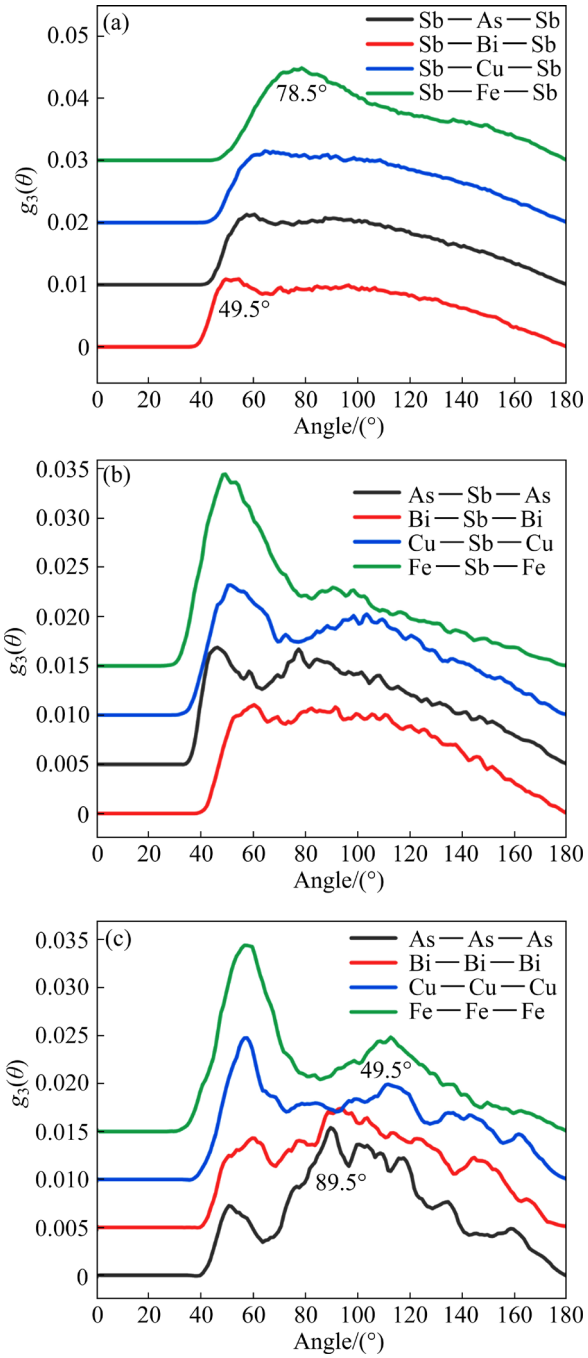

Fig. 8 Bond angle distribution in molten $Sb_{88}X_{20}$ (X=As, Bi, Cu, Fe) alloy at 1600 K: (a) Sb—X—Sb bond angle; (b) X—Sb—X bond angle; (c) X—X—X bond angle

The experimental and computational results from the previous studies [21,40,41] on pure Sb melt indicate that the bond angle distribution of the pure antimony melt exhibits two prominent peaks.

The first peak, corresponding to smaller angles, is located around 57°, while the second peak, at a larger angle, is expected to be around 90°. Figure 8(a) shows the distribution of Sb—X—Sb bond angles. As can be seen from Fig. 8(a), among all the bond angle distributions, the AA for Sb—As—Sb is 57° and the OA is 88°, which closely resembles the bond angle distribution of pure Sb melt. Next is Sb—Bi—Sb, with an AA of 54° and an OA of 84°, which also closely matches the bond angle distribution of pure Sb melt. However, the AA and OA for Sb—Cu—Sb and Sb—Fe—Sb bond angles are both greater than the corresponding bond angle distribution of pure Sb melt. In particular, the AA and OA for Sb—Fe—Sb show a more significant difference when compared to the AA and OA of pure Sb melt. This phenomenon suggests that the local topological order around the solute atoms Cu and Fe differs significantly from that of the pure Sb melt, whereas the local topological order around the solute atoms Bi and As becomes increasingly similar to that of pure Sb melt.

As shown in Fig. 8(b), in the BADFs of Fe—Sb—Fe and Cu—Sb—Cu, the intensity of the AA is higher than that of OA. This phenomenon indicates that in the corresponding structures, Fe—Sb—Fe and Cu—Sb—Cu are more likely to form acute bond angles. In contrast, in the BADFs of Bi—Sb—Bi and As—Sb—As, the intensities of AA and OA are relatively close. This suggests that in the Sb melt, Bi—Sb—Bi and As—Sb—As do not tend to form a specific bond angle. Figure 8(c) shows the BADFs of X—X—X angles. As can be seen, in BADFs of As—As—As and Bi—Bi—Bi, the intensity of the AA is weaker than that of OA. Moreover, the large-angle bond angles exhibit relatively high noise during the statistical process. This indicates that the probabilities of the above two types of bond angles occurring in the melt are relatively low during the statistical process, which further demonstrates the tendency of As and Bi atoms to disperse rather than agglomerate in the Sb melt. In contrast, the noise in the BADFs of Fe—Fe—Fe and Cu—Cu—Cu is significantly lower than that in other systems. This implies that the probabilities of these two types of bond angles are relatively high during the statistical process, thus further confirming that Fe and Cu atoms are more likely to form aggregates in the melt. Among them, the intensity of the first peak of the bond angles of Fe—Fe—Fe and Cu—Cu—Cu is stronger than that of the second peak. This suggests that Fe and Cu atoms form relatively compact clusters in the melt.

3.6 Voronoi polyhedron (VP) analysis

To further investigate the differences in the local atomic topological structures around various solute atoms in the Sb melt, this study employs the Voronoi tessellation [42,43] method to examine the detailed geometric structures of the central solute atoms and their neighboring atoms in the molten state. The VP is centered around the solute atom, with its boundaries formed by the perpendicular bisectors between the central atom and its neighboring atoms. Different types of VP are distinguished by Voronoi indices $\langle n_3, n_4, n_5, \cdots \rangle$, where n_i represents the number of faces with i edges. The number of faces of a VP corresponds to the coordination number. For example, $\langle 0, 0, 12, 0 \rangle$ represents an ideal icosahedron, which contains 12 pentagonal faces [44].

Figure 9 illustrates the most abundant types of VP centered around solute atoms As, Bi, Cu, and Fe in Sb melt at four different temperatures. Although some VP types are not consistently the most abundant across all temperatures, they remain among the most frequently occurring types under other temperature conditions. This phenomenon suggests the presence of a distinct evolutionary order within the liquid structure. Furthermore, the composition of these VP types effectively reflects the local structural characteristics centered on different solute atoms in the Sb melt. In the Sb melt, the most favorable types of VP centered around different solute atoms are $\langle 0, 0, 0, 4, 4, X \rangle$ and $\langle 0, 0, 0, 3, 6, X \rangle$.

Comparative analysis reveals that the VP fractions surrounding As and Bi atoms are lower than those around Cu and Fe atoms, and the VP face distributions for As and Bi atoms are more complex. This indicates that the atomic arrangements around As and Bi exhibit greater irregularity. Additionally, a larger number of edges typically suggest a relatively looser local environment for the central atom. The significant differences in VP types can be attributed primarily to the chemical effects within the melt. Furthermore, the VP analysis centered on solute atoms shows that with increasing

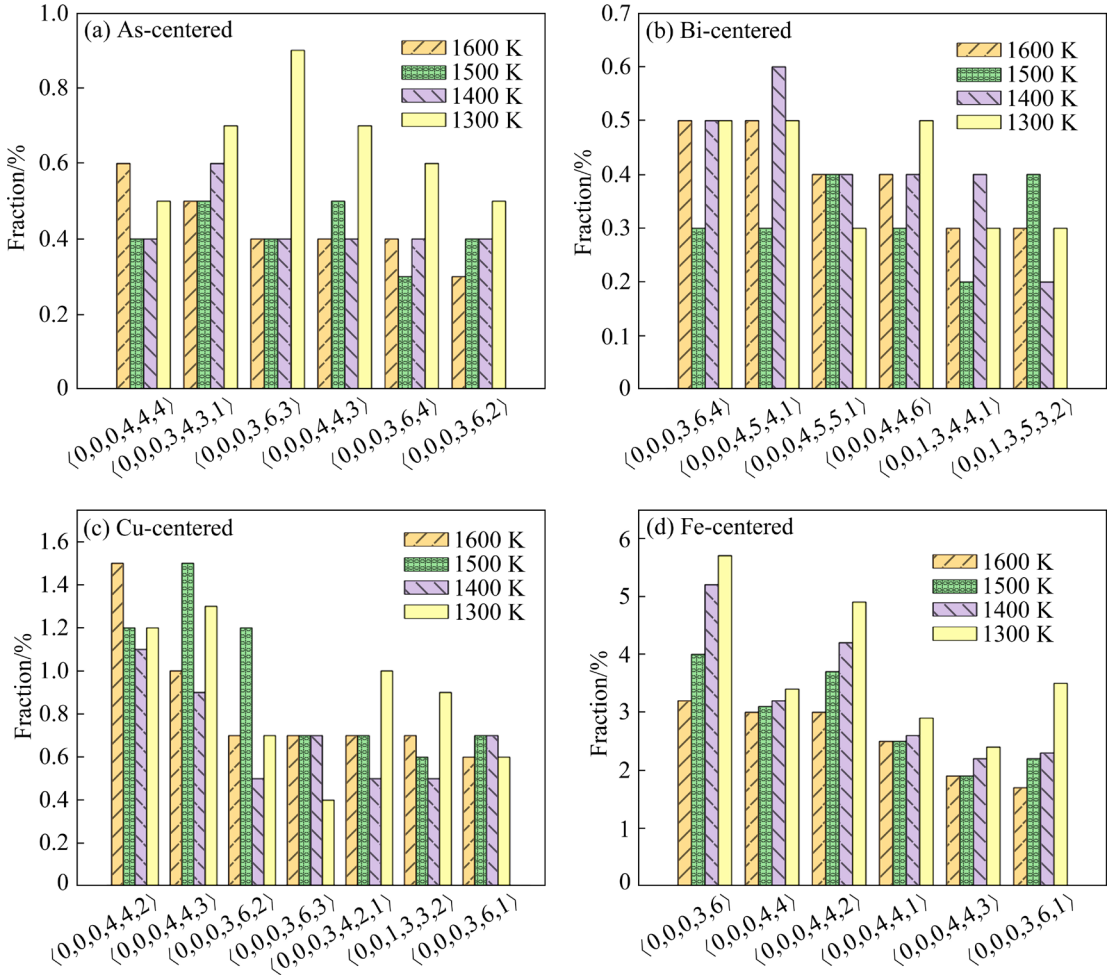

Fig. 9 VP analysis of various solute atoms (As, Bi, Cu, and Fe) as function of temperature in Sb melt

temperature, the fractions of all VP types decrease, indicating that melt becomes more homogeneous at higher temperatures.

3.7 Dynamical properties

The interactions of solute atoms in the melt inevitably influence their diffusion behavior, and the diffusion of solute atoms in the melt is also a critical factor affecting segregation efficiency. In this study, the diffusion behavior of solute atoms As, Bi, Cu, and Fe in Sb melts is further investigated. The diffusion coefficients of solute atoms are calculated using methods based on the mean square displacement (MSD) (Eq. (5)) and the velocity auto-correlation functions (VAF) (Eq. (6):

$$D=\lim_{t\to\infty}\frac{\left\langle\sum_{i=1}^{N}\left|r_i(t)-r_i(0)\right|^2\right\rangle}{6Nt} \tag{5}$$

$$D=\frac{1}{3N}\int_0^{\infty}\sum_{i=1}^{N}\left\langle V_i(t)\cdot V_i(0)\right\rangle \mathrm{d}t \tag{6}$$

The definitions of Eq. (5) and Eq. (6) are fully consistent with the corresponding formulas in Refs. [39,45]. To provide a more accurate characterization of the diffusion coefficient, this study divides the entire calculation process into 800 smaller steps. Specifically, the diffusion coefficient is computed every 800 steps (corresponding to a time duration of 2.4 ps), and the average of these calculated values is then taken. The MSD and VAF curves for As, Bi, Cu, and Fe in the Sb melt at 1600 K are presented in Fig. 10.

In studying the diffusion behavior of solute atoms in the Sb melt, the VAF serves as an important analytical tool. A negative value of the VAF indicates that the moving atoms are “trapped” and “rebounded” by their nearest neighbors, a phenomenon known as the “cage effect” [46]. From the VAF results, it is evident that the “cage effect” is most pronounced in the region surrounding Fe atoms. To further investigate the diffusion

characteristics of solute atoms (As, Bi, Cu, and Fe) in the Sb melt, this study employs both the MSD and the VAF methods. Figure 11 presents the temperature dependence of the diffusion coefficients of the solute atoms in the Sb melt, as calculated using these two methods. A comparison reveals that the self-diffusion coefficients obtained from the VAF method are in close agreement with those calculated from the MSD method. However, since the VAF method more heavily considers atomic motion within the spherical shell, the results obtained using VAF tend to be slightly higher than those obtained from MSD. This discrepancy is attributed to the inherent differences between the two calculation methods. The diffusion coefficient results shown in Fig. 11 indicate that, in Sb melt, the diffusion coefficients of the solute atoms As, Bi, Cu, and Fe decrease with decreasing temperature. Among them, the diffusion coefficient of Fe atoms is the smallest. This finding further suggests that the cluster structure surrounding Fe atoms is the most compact, and correspondingly, the “cage effect” is the strongest in this region.

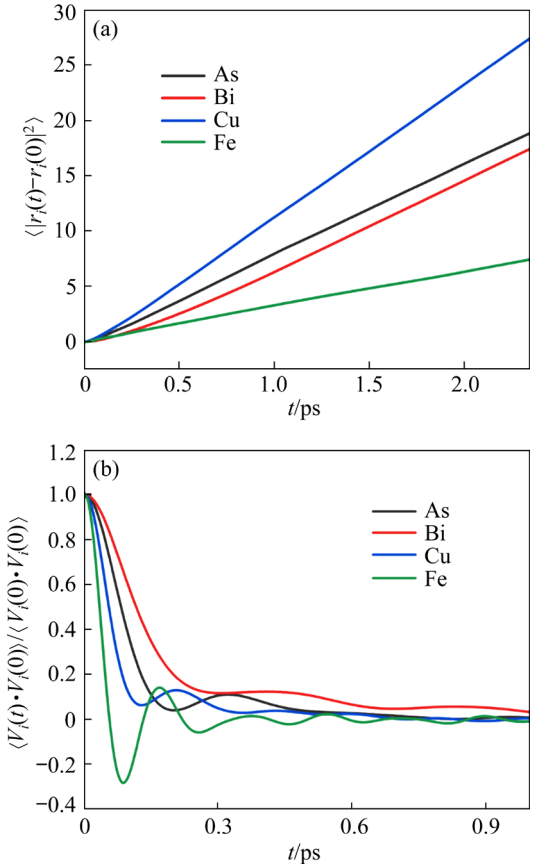

Fig. 10 MSD (a) and VAF (b) curves for solute atoms As, Bi, Cu, and Fe in Sb melt at 1600 K

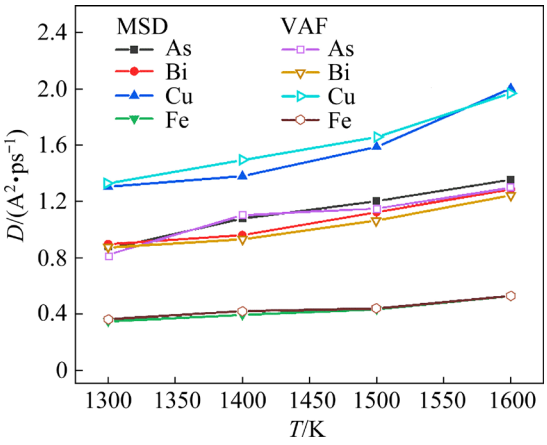

Fig. 11 Diffusion coefficients of As, Bi, Cu, and Fe as function of temperature calculated by MSD and VAF methods

4 Conclusions

(1) This study employs AIMD simulations to investigate the local structures and dynamical properties of solute atoms As, Bi, Cu, and Fe in liquid Sb, focusing on the two typical segregation behaviors of these solute atoms. Their segregation behavior in liquid metal Sb shows significant differences. The results reveal correlations between the chemical effects and the segregation behavior of the solute elements in the Sb melt.

(2) In Sb melt, solute atoms Cu and Fe, which have smaller distribution coefficients, show a stronger affinity for Sb than As and Bi, which have larger distribution coefficients. As a result, As and Bi exhibit weaker interactions with Sb and a more disordered distribution within the melt. These differences in affinity significantly affect the segregation behavior and local structure of the Sb alloy. The Sb−Fe system features a unique 1551 bond, forming an L-FFS structure, which slows down the Fe atom diffusion and promotes the compact cluster formation, further hindering the solute diffusion. Overall, the differences in chemical bonding among these elements play a key role in determining the local structure and diffusion properties of the melt.

(3) Bond angle analyses reveal that in the Sb−As and Sb−Bi solutions, the distribution closely resembles that of pure Sb melt, while Sb−Cu and Sb−Fe solutions show significant differences. Additionally, the Fe—Sb—Fe and Cu—Sb—Cu

solutions tend to form acute bond angles. The VP types reflect local structural features, with the most common being ⟨0, 0, 0, 4, 4, *X*⟩ and ⟨0, 0, 0, 3, 6, *X*⟩ around the solutes in the Sb melt. The VP fractions around As and Bi are lower and more irregular compared to those around Cu and Fe, indicating a more disordered atomic arrangement. The smallest diffusion coefficient is observed for Fe, whose localized compact structure significantly hinders its mobility.

CRediT authorship contribution statement

Zong-bo LI: Validation, Formal analysis, Investigation, Resources, Writing − Original draft, Writing − Review & editing; **Yan FENG:** Methodology, Conceptualization, Formal analysis, Supervision, Project administration, Funding acquisition, Resources; **Ze-hang ZHUANG:** Validation, Formal analysis, Writing − Review & editing; **Xiang PENG:** Methodology, Conceptualization, Writing − Review & editing, Visualization, Supervision, Funding acquisition, Resources; **Ri-chu WANG:** Validation, Formal analysis, Writing − Review & editing.

Declaration of competing interest

The authors declare that they have no known competing financial interests or personal relationships that could have appeared to influence the work reported in this paper.

Acknowledgments

The authors express their gratitude to the computational resources supplied by the High Performance Computing Cluster (HPC) at Central South University, China.

References

[1] SHAKOURI A. Recent developments in semiconductor thermoelectric physics and materials [J]. Annual Review of Materials Research. 2011, 41(1): 399−431.

[2] CHIN H S, CHEONG K Y, RAZAK K A. Review on oxides of antimony nanoparticles: Synthesis, properties, and applications [J]. Journal of Materials Science, 2010, 45: 5993−6008.

[3] MENG Chao-song, YANG Huan, WEI Xiao-hui, XU Chang-yi, ZENG Yuan-lin, XIONG Heng, YANG Bin, XU Bao-qiang. A novel process for directional impurity removal and preparation of front-end high-purity antimony from crude antimony [J]. Vacuum, 2024, 219: 112736.

[4] LI Ya-xing, LI Zong-bo, WANG Ri-chu, PENG Chao-qun, FENG Yan, WANG Xiao-feng, CAI Zhi-yong. The separation behavior of impurity in antimony during vacuum distillation [J]. Vacuum, 2023, 211: 111669.

[5] ZHANG Xiao-xin, FRIEDRICH S, FRIEDRICH B. Separation behavior of arsenic and lead from antimony during vacuum distillation and zone refining [J]. Journal of Materials Research and Technology, 2020, 9(3): 4386−4398.

[6] ZUO Zi-bin, ZHU Rong-bo, LIU Xin-yang, CHEN Xiu-min, SHI Teng-teng, LEI Xian-jun, WU Jian, JIANG Wen-long, YANG Bin, XU Bao-qiang. Separation of arsenic and antimony: A comprehensive theoretical and experimental study [J]. Journal of Materials Research and Technology, 2024, 31: 1080−1090.

[7] XU Chang-yi, ZENG Yuan-lin, WANG Zhao-yi, DONG Zhao-wang, XIONG Heng, XU Bao-qiang, YANG Bin, JIANG Wen-long, DONG Jing-cheng, HE Yu-hong. The volatilization law of standard impurity elements in 3N antimony during vacuum distillation and preparing antimony with 4N8 content [J]. Separation and Purification Technology, 2025, 355: 129675.

[8] YANG Jian-guang, WU Yong-tian. A hydrometallurgical process for the separation and recovery of antimony [J]. Hydrometallurgy, 2014, 143: 68−74.

[9] IYER R K, DESHPANDE S G. Preparation of high-purity antimony by electrodeposition [J]. Journal of Applied Electrochemistry, 1987, 17: 936−940.

[10] ZHENG Lin, ZHANG Lei, ZHOU Yi, SUN Yan-rong, NAN Chang-bin, ZHOU Xi-ping, QIN Shi-min, SHI Hua-feng, LI Jia-xuan, XU Bao-qiang. New approach to predict impurity concentration in high-purity antimony metal prepared by vacuum distillation [J]. Vacuum, 2024, 226: 113285.

[11] ZHANG Xiao-xin, FRIEDRICH S, LIU Bin, HUANG Tian-xiang, FRIEDRICH B. Computation-assisted analyzing and forecasting on impurities removal behavior during zone refining of antimony [J]. Journal of Materials Research and Technology, 2020, 9(2): 1221−1230.

[12] HU Dong-liang, GU Xing-yu, LYU Lei, PEI Jian-zhong, CUI Bing-yan. Investigating the aging mechanism of asphaltene and its dependence on environmental factors through AIMD simulations and DFT calculations [J]. Science of the Total Environment, 2021, 795: 148897.

[13] ZHANG Yong, MAGINN E J. A simple AIMD approach to derive atomic charges for condensed phase simulation of ionic liquids [J]. The Journal of Physical Chemistry B, 2012, 116(33): 10036−10048.

[14] HAO Qing-hai, LI Y D, KOONG Xiang-shan, LIU C S. Ab initio molecular dynamics simulations on local structure and electronic properties in liquid Sb from 913 K to 1193 K [J]. International Journal of Modern Physics B, 2013, 27(5): 1350012.

[15] LI Zong-bo, FENG Yan, WEN Yu-feng, PENG Xiang, CAI Zhi-yong, PENG Chao-qun, WANG Ri-chu. Ab initio molecular dynamics study on the local structures and solid/liquid interface in liquid Al−Ti and Al−B−Ti alloys [J]. Materials Today Communications, 2024, 39: 109290.

[16] HAFNER J. Ab-initio simulations of materials using VASP: Density-functional theory and beyond [J]. Journal of Computational Chemistry, 2008, 29(13): 2044−2078.

[17] BOTTON G A, HUMPHREYS C J. Determining the

bonding in intermetallics using electron energy loss spectroscopy and density functional theory [J]. Intermetallics, 1999, 7(7): 829−833.

[18] BLGHOL P E. Projector augmented-wave method [J]. Physical Review B, 1994, 50(24): 17953.

[19] HAMMER B, HANSEN L B, NORSKOV J K. Improved adsorption energetics within density-functional theory using revised Perdew−Burke−Ernzerhof functionals [J]. Physical Review B, 1999, 59(11): 7413.

[20] PERDEW J P, BURKE K, ERNZERHOF M. Generalized gradient approximation made simple [J]. Physical Review Letters, 1996, 77(18): 3865.

[21] LI Zong-bo, LI Ya-xing, FENG Yun, FENG Yan, WEN Yu-feng, WANG Ri-chu, PENG Chao-qun, CAI Zhi-yong. Ab initio molecular dynamics study of the local structures and migration behaviors of liquid Sb-based alloys [J]. Journal of Physics D: Applied Physics, 2023, 57(11): 115303.

[22] BRAGA C, TRAVIS K P. A configurational temperature Nosé-Hoover thermostat [J]. The Journal of Chemical Physics, 2005, 123: 134101.

[23] FENG Yun, FENG Yan, LI Zong-bo, PENG Hai-long. Chemically ordered structure and dynamics in Al80Ti20 liquids [J]. Computational Materials Science, 2023, 226: 112256.

[24] YANG Jian, MA Jian-bo, CHEN Shi-hao, ZHANG Jiao, DAI Yong-bing, FU Chao-peng, SUN Bao-de. The correlation between chemical effect and segregation behavior in metallic Al liquid [J]. Computational Materials Science, 2020, 175: 109611.

[25] LI Zong-bo, XIONG Kai, SUN Ying-jie, JIN Cheng-chen, ZHANG Shun-meng, HE Jun-jie, MAO Yong. First-principles study of mechanical and thermodynamic properties of intermetallic Pt3M (M= Al, Hf, Zr, Co, Y, Sc) [J]. Computational Condensed Matter, 2020, 23: e00462.

[26] MA Jian-bo, SHANG Sun-li, KIM H, LIU Zi-kui. An ab initio molecular dynamics exploration of associates in Ba−Bi liquid with strong ordering trends [J]. Acta Materialia, 2020, 190: 81−92.

[27] CHHEN Shi-hao, WANG Shu-bin, LIANG Hong-tao, MA Jian-bo, HU Guang-min, DAI Yong-bing, YANG Jian, ZHANG Jiao, YANG Yang, SUN Bao-de. Element interactions and local structure in molten NiRe and NiAlRe alloys: Implications for the aggregation and partition of Re [J]. Acta Materialia, 2020, 188: 344−353.

[28] CHEN Shi-hao, MA Jian-bo, DAI Yong-bing, YANG Jian, ZHANG Jiao, DONG Qing, HAN Yan-feng, XING Hui, SUN Bao-de. Atomic-scale simulations of the local structures of molten $Ni_{1-x}Co_x$ and $Ni_{1-x}Fe_x$ [J]. Journal of Non-crystalline Solids, 2018, 481: 470−478.

[29] VOIGTMANN T, MEYER A, HOLLAND M D, STUBER S, HANSEN T, UNRUH T. Atomic diffusion mechanisms in a binary metallic melt [J]. Europhysics Letters, 2008, 82(6): 66001.

[30] QIN Jing-yu, BIAN Xiu-fang, SLIUSARENKO S I, WANG Wei-min. Pre-peak in the structure factor of liquid Al−Fe alloy [J]. Journal of Physics: Condensed Matter, 1998, 10(6): 1211.

[31] XU Chuang, CHEN Yun, GONG Tong-zhao, SHI Yong-peng, WANG Jian-tao, CHEN Xing-qiu, LIU Pei-tao, GUO Yi, LI Dian-zhong. Ab initio study of local structures during cooling of liquid Fe−C and Fe−Cr−C alloys [J]. Computational Materials Science, 2022, 212: 111572.

[32] CELTEK M. An in-depth investigation of the microstructural evolution and dynamic properties of Zr77Rh23 metallic liquids and glasses: A molecular dynamics simulation study [J]. Journal of Applied Physics, 2022, 132: 035902.

[33] JAKSE N, PASTUREL A. Dynamic properties and local order in liquid Al−Ni alloys [J]. Applied Physics Letters, 2014, 105: 131905.

[34] WAGNER C, RUPPERSBERG H. Neutron and X-ray diffraction studies of the structure of metallic glasses [J]. Atomic Energy Review, 1981(Supplement 1): 101−141.

[35] YANG Jian, ZHANG Jiao, DAI Yong-bing, MA Jian-bo, LI Fa-guo, BIAN Feng-gang, MI Jia-wei, SUN Bao-de. Ab initio simulation: The correlation between the local melt structure and segregation behavior of Fe, V, Ti and Si in liquid Al [J]. Computational Materials Science, 2015, 109: 41−48.

[36] SHI Yong-peng, LIU Ming-feng, WANG Jian-tao, MA Hui, LI Rong-han, CHEN Yun, MO Wen-lin, LI Dian-zhong, BAI Bin, WANG Xiao-lin. Localized Nb clusters in U−Nb liquid alloys: An ab initio molecular dynamics study [J]. Nuclear Materials and Energy, 2021, 26: 100915.

[37] CHENG Y Q, SHENG H W, MA E. Relationship between structure, dynamics, and mechanical properties in metallic glass-forming alloys [J]. Physical Review B—Condensed Matter and Materials Physics, 2008, 78(1): 014207.

[38] FENG Yun, FENG Yan, PENG Hai-Long. Ab initio study of chemical effect on structural properties of Ti−Al melts [J]. Chinese Physics B, 2023, 32(10): 106101.

[39] MA Jian-bo, DAI Yong-bing, ZHANG Jiao, ZHANG Zhen-lei, WANG Jun, SUN Bao-de. Ab initio molecular dynamics study of the structure of undercooled Ni melt [J]. Journal of Non-crystalline Solids, 2013, 376: 216−220.

[40] WANG Q, LI C X, WU Z H, WANG L W, NIU X J, YAN W S, XIE Y N, WEI S Q, LU K Q. Temperature effect of the local structure in liquid Sb studied with X-ray absorption spectroscopy [J]. The Journal of Chemical Physics, 2008, 128: 224501.

[41] BICHARA C, PELLEGATTI A, GASPARED J P. Properties of liquid group-V elements: A numerical tight-binding simulation [J]. Physical Review B, 1993, 47(9): 5002.

[42] WANG W Y, HAN J J, FANG H Z, WANG J, LIANG Y F, SHANG S L, WANG Y, LIU X J, KECSKES L J, MATHAUDHU S N. Anomalous structural dynamics in liquid $Al_{80}Cu_{20}$: An ab initio molecular dynamics study [J]. Acta Materialia, 2015, 97: 75−85.

[43] DU Qiang, FABER V, GUNZBURGER M. Centroidal Voronoi tessellations: Applications and algorithms [J]. SIAM Review, 1999, 41(4): 637−676.

[44] LAZAR E A, MASON J K, MACPHERSON R D, SROLOVITZ D J. Statistical topology of three-dimensional Poisson-Voronoi cells and cell boundary networks [J]. Physical Review E, 2013, 88(6): 063309.

[45] MA Jian-bo, DAI Yong-bing, ZHANG Jiao, CHEN Shi-hao,

YANG Jian, XING Hui, DONG Qing, HAN Yan-feng, SUN Bao-de. On the chemical effects in molten $Ni_{1-x}M_x$ alloy [J]. Computational Materials Science, 2018, 146: 158−175.

[46] PASCHOAL V H, FARIA L F, RIBEIRO M C. Vibrational spectroscopy of ionic liquids [J]. Chemical Reviews, 2017, 117(10): 7053−7112.

从头算分子动力学(AIMD)研究液态锑基合金化学效应与偏析行为的相关性

栗宗波[1,2]，冯 艳[1,2]，庄泽航[1,2]，彭 翔[1,2]，王日初[1,2]

1. 中南大学 材料科学与工程学院，长沙 410083；
2. 中南大学 高强结构材料科学与技术国家重点实验室，长沙 410083

摘 要：选取在液态 Sb 合金中表现出两类典型偏析行为的溶质原子(As、Bi)与(Cu、Fe)进行分析。采用从头算分子动力学(AIMD)模拟研究不同温度下的液态 Sb 合金。通过分析双体相关函数(PCF)、键对、键角分布函数(BADF)和 Voronoi 多面体(VP)，考察了合金熔体的短程有序(SRO)。在 Sb 熔体中，分配系数较小的溶质原子 Cu 和 Fe 较分配系数较大的 As 和 Bi 对 Sb 表现出更强的亲和性。分配系数较大的 As 和 Bi 的 BADF 显示小角度峰的概率低于大角度峰，而分配系数较小的 Cu 和 Fe 则呈相反趋势。BADF 表明 Sb−As 和 Sb−Bi 接近纯 Sb 熔体的特征，而 Sb−Cu 和 Sb−Fe 则明显偏离。与 Sb−Cu 和 Sb−Fe 相比，Sb−As 和 Sb−Bi 体系表现出更多低指数键对，表明相互作用较弱且结构更无序。As 和 Bi 原子周围的 Voronoi 多面体占比低于 Cu 和 Fe 周围，且 As 和 Bi 周围多面体的面数分布更为复杂。不同溶质原子周围的 Voronoi 多面体存在差异，这主要归因于各溶质原子对应的键对分数不同。Fe 具有最小的扩散系数，这主要归因于其局域结构更为紧密。

关键词：AIMD；偏析；液态 Sb 基合金；短程有序；As；Bi；Cu；Fe

(Edited by Bing YANG)